



Assessment of structural, optical, magnetic, magnetocaloric properties and critical phenomena of $\text{La}_{0.57}\text{Nd}_{0.1}\text{Sr}_{0.18}\text{Ag}_{0.15}\text{MnO}_3$ system at room temperature

S. Gharbi¹ · Y. Marouani¹ · F. Issaoui² · E. Dhahri¹ · E. K. Hlil³ · R. Barille⁴ · B. F. O. Costa⁵

Received: 26 March 2020 / Accepted: 9 June 2020
© Springer Science+Business Media, LLC, part of Springer Nature 2020

Abstract

In this research paper, our central focus is upon structural, optic, magnetic, magnetocaloric, and critical phenomena of $\text{La}_{0.57}\text{Nd}_{0.1}\text{Sr}_{0.18}\text{Ag}_{0.15}\text{MnO}_3$ (LNSMAO) compound. This compound is crystallized in the rhombohedral system, with a $R\bar{3}c$ space group. The band gap energy of this powder was 2.5 eV. Therefore, the LNSAMO sample proved to be not only a photocatalysis material but also a photovoltaic application. The FTIR spectra confirmed the formation of the structure of orthorhombic perovskite. The second-order transition of the magnetic phase in the LNSMAO sample was also reported by the positive slopes of the Arrott plot. Beneath 5 T, the values of magnetic entropy change and relative cooling power, respectively, amounted to about $5.08 \text{ J kg}^{-1} \text{ K}^{-1}$ and 146.7 J/Kg . In perspective, this sample stands for an agreeable candidate for magnetic refrigeration. By analyzing the dependence on the field of the magnetic entropy change (ΔS_M) data as well as the relative cooling power (RCP), it was possible to assess the values of the critical exponents. Moreover, the critical exponents of LNSMAO compound were estimated based on multiple techniques like Kouvel-Fisher (KF), modified Arrott plot (MAP) method, and critical isotherm analysis (CIA). The reliability of these critical behaviors was verified by the Widom scaling relation and the universal scaling hypothesis. Our results demonstrate an excellent correlation between magnetocaloric effect (MCE) properties in manganese systems and critical behavior.

1 Introduction

Nowadays, human needs of a lot of energy push the discovery new energy-economic technologies such as cooling technology since it has one of the utmost energy consumption rates in residential and commercial areas. The existence of forward magnetic refrigeration technologies has lately

produced enormous interest in research; the apparatus operates at room temperature and in a small magnetic field [1–3]. The hole-doped lanthanum manganites oxides systems have a general formula of the type $\text{Ln}_{1-x}\text{A}_x\text{MnO}_3$ with Ln as a rare earth (La, Nd), A is an alkaline earth (Ca, Sr, Ba) or an alkali (K, Na, Ag). These manganites were explored essentially in 1993 following the discovery of colossal magnetoresistance (CMR) in thin films of $\text{La}_{1-x}\text{Ca}_x\text{MnO}_3$ [4, 5]. These compounds admit a variety of properties, explaining their interest in the world of research [6–10], such as electronic, structural, and magnetic properties, and their interpretation in theoretical fields and also for very interesting applications (magnetic recording, magnetic refrigeration, resistive magnetic sensors, etc.). The finding of the magnetocaloric effect [11–15] is the basis of magnetic refrigeration which can substitute Classical vapor Compression (CVC) systems [16, 17] that are more energy-intensive and environmentally harmful [18].

The first observation of the magnetocaloric effect (MCE), thus, dates back to nearly 130 years when in 1881 the German physicist Emil Warburg discovered it in iron [19]. The MCE is a physical property of the magnetic material

✉ S. Gharbi
azzouzi.sirine@outlook.com

¹ Laboratory of Applied Physics, Faculty of Science, University of Sfax, B.P. 1171, 3000 Sfax, Tunisia

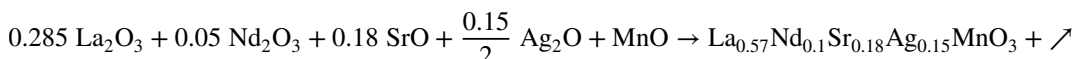
² Research Unit Development and Optimization of the Exploitation of Resources, Faculty of Science and Technology of Sidi Bouzid, University of Kairouan, 9100 Sidi bouzid, Tunisia

³ CNRS, University Grenoble Alpes, BP 166, 38042 Grenoble Cedex9, France

⁴ MOLTECH-Anjou, University of Angers/UMR CNRS 6200, 2 Boulevard Lavoisier, 49045 Angers, France

⁵ Department of Physics, CFisUC, University of Coimbra, Rua Larga, 3004-516 Coimbra, Portugal

consisting of a heating or cooling (both reversible) of the material around its Curie temperature beneath the action or elimination of an external magnetic field [20]. This effect is based on the intrinsic properties of magnetic materials and is viewed by an adiabatic variation of the temperature ΔT or a variation of the magnetic entropy ΔS . The determination of ΔS is deduced indirectly from magnetization measurements or by specific magnetic heat data [21, 22]. There are



two different types of magnetic entropy changes, one for ferromagnetic materials, the change of $\Delta S(T)$ is positive with a maximum (normal magneto-electric effect) in the proximity of Curie temperature (T_C) [16, 23–25]. The other for the antiferromagnetic materials, there is a change from a positive increase to a negative increase of ΔS around the temperature of Néel (T_N), showing its large inverse magnetocaloric effect (IMCE) [20].

The substitution, on site A or B of manganites, was studied in order to modify the $\text{Mn}^{3+}/\text{Mn}^{4+}$ ratio, as well as the magnetic interactions within the structure in order to better understand the impact of these interactions on the physical properties manganites which causes a transition from the paramagnetic(PM) insulator to the ferromagnetic(FM) metallic phase. For this reason, there are two questions about a (PM)-(FM) transition: the first about the phase transition order and the second deals with the class of common universality. Hence, it is intrinsic to study the critical behavior of manganites in the (PM)-(FM) transition zone around T_C [26] for investigating the nature of first- or second-order magnetic transition and to identify magnetic susceptibility γ (varies between 1 and 1.4) and critical magnetization β (varies in the range 0.3–0.5). The discovery of critical phenomena in manganites attracted a lot of interest in the early 1990 [27]. There are four different types of theoretical models: mean-field model ($\beta=0.5, \gamma=1$) [28], Ising 3D model ($\beta=0.325, \gamma=1.240$) [29, 30], Tricritical model ($\beta=0.25, \gamma=1$), and Heisenberg 3D model ($\beta=0.365, \gamma=1.336$) [31, 32].

In this work, we are basically concerned with the structural, optical, magnetic, critical phenomena, and MEC of the sample LNSAMO synthesized by the solid-state method. We as well address the dependence on the field of the change of ΔS_M as well as the RCP. Critical behavior is tackled using two methods: The first method rests upon magnetic entropy change data as much as relative cooling power, whereas the second method is based on modified Arrott plots predicated on static magnetic measurement data using different techniques like KF, MAP, and CIA.

2 Experimental techniques

The powder of LNSMAO compound was synthesized using the conventional solid–solid reaction in air. The used precursors are lanthanum oxides La_2O_3 , neodymium oxide Nd_2O_3 , manganese oxide MnO , strontium oxide SrO , and silver oxide Ag_2O . The precursors which admit purity up to 99.9% are mixed in the preferred proportions according to the subsequent reaction:

Subsequently, the powder was blended, grounded, and after that calcined at 950 °C for 24 h. The calcined blend was reground, blended properly, compressed into pellets (10 mm of diameter and about 1 mm of thickness), and fritted at 1373 K for 24 h and 1573 K for 13 h with grinding between the two fritting temperatures. The elaborated compound was evaluated by X-ray diffraction (XRD) utilizing a Siemens D5000 diffractometer equipped with $\text{CuK}_{\alpha 1}$ radiation ($\lambda_{\text{Cu}} = 1.5406 \text{ \AA}$) and a graphite back monochromator. The recording of X-ray powder diagrams was performed out at room temperature in an angular range of 10°–100° with a pitch of 0.02°. The crystalline parameters of the studied compound were refined with the Reitveld method utilizing the FULLPROF program [33]. Surface morphology of this material was examined by Scanning Electron Microscopy (SEM). Infrared spectra were recorded at ambient temperature with a Perkin Elmer spectrophotometer in the wave number interval 500–4000 cm^{-1} . UV–Vis spectra of investigated compound was performed at room temperature using UV-3101PC scanning spectrophotometer (Integrated Sphere) in the range of wavelength (200–1000) nm. Magnetic measurements of the LNSAMO sample versus the temperature beneath a weak field of about 0.05 T were conducted using a BS2 magnetometer.

3 Results and discussion

3.1 Crystal structure

Figure 1 plots XRD pattern of LNSAMO at room temperature. Utilizing the Reitveld powder diffraction profile fitting technique, we investigated the diffraction data so as to get the structural parameters. LNSMAO Sample crystallizes in an only phase with slight traces of Mn_3O_4 . For a rhombohedra structure with $R\bar{3}c$ space group, where we find that the La/ Sr /Nd /Ag atoms are at 6a (0, 0, 1/4), Mn at 6b (0, 0, 0), and O at 18e (x, 0, 1/4) positions,

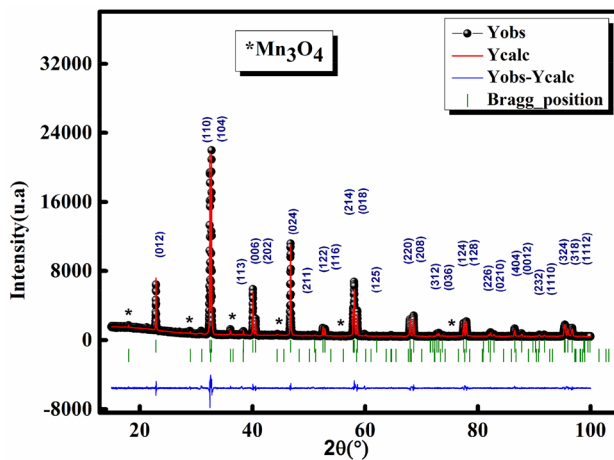


Fig. 1 Refined X-ray diffraction patterns of LNSAMO compound: Solid black circle represents the observed pattern; continuous red line represents computed pattern, and the blue line represents distinction between the observed and computed patterns. Tick green markers correspond to the position of the allowed Bragg diffractions (Color figure online)

Table 1 Refined structural parameters of LNSAMO compound

Sample	$La_{0.57}Nd_{0.1}Sr_{0.18}Ag_{0.15}MnO_3$	
Space group	$R\bar{3}\ c$	I41/amd
a (Å)	5.512(9)	5.768(1)
b (Å)	5.512(9)	5.768(1)
c (Å)	13.334(2)	9.376(1)
V(Å ³)	58.49	77.99
Discrepancy factors		
R_{wp} (%)	6.90	
R_p (%)	6.90	
R_{exp} (%)	3.63	
χ^2	3.12	
Bond angles and bond lengths		
$\langle Mn-O-Mn \rangle$ (°)	164.19(8)	
$\langle d_{(Mn-O)} \rangle$ (Å)	1.961(9)	
D_{sc} (nm)	26	
D_{Meb} (μm)	0.533	

we notice that the diffraction peaks are net and can be classified. We have determined the detailed results of the structural refinements utilizing the Reitveld evaluation of the XRD data with the FULLPROF software and they are displayed in Table 1. The remaining for the pattern R_{wp} , the weighted pattern R_p , the structure factor RF, and the goodness of fit χ^2 are as well tabulated in Table 1. Final RF of refinements was all the time less than 4.01%, which is analogous to those results established in the literature [34]. The mean crystallite (D_{SC}) was computed from the XRD patterns, utilizing the Scherer's formula [35]:

$$D_{SC} = \frac{k \times \lambda}{\beta \times \cos\theta} \quad (1)$$

where λ corresponds to the applied wavelength, β corresponds to the full width half maximum intensity (FWHM), and θ corresponds to the Bragg angle for the most intense peak. The mean value of the crystallite sizes was found to be around 26 nm.

3.2 Energy-dispersive analysis and scanning electron microscope

So as to check the presence of each element in the (LNSAMO) compound, energy dispersive X-ray analysis (EDX) was carried. The EDX spectrum depicted in Fig. 2a shows the existence of Nd, La, Sr, Ag, and Mn, which confirms that there is no beating of elements in the sintering. The EDX analysis demonstrates that the chemical elements of this compound are near to the nominal ones. The surface morphology of the material is explored by SEM. Figure 2 portrays the SEM micrographs at room temperature of the compound LNSAMO. A manual statistical count of the particle size was carried out on this image utilizing the ImageJ software. The results are recorded in Fig. 2c as grain number (counts) versus particle size (μm) of LNSAMO compound. The histogram outlines grain size dispersion that follows Lorentzienne law (red continuous line) for the sample. The computed mean grain size is around 0.533 μm. We noticed that the mean grain size values calculated from the micrographs are considerably superior to those indicated by XRD data. This distinction is assigned to the fact that each particle seen by SEM is formed by many crystallized grains [36] (see Table 1).

3.3 Optical property

3.3.1 FTIR spectroscopy

The FTIR spectra of LNSAMO compound recorded at ambient temperature in the wave number range (500–4000) cm⁻¹ is reported in Fig. 3a. The FTIR spectrum is a technique that indicates the presence of frequency bands owing to ion vibrations in the network. The bands are observed at 454 cm⁻¹, 584 cm⁻¹, and 2350 cm⁻¹. The vibration band around 584 cm⁻¹ is attributed to the stretching mode which entails the interior movement of a modification in length of the Mn–O bond and the band about 454 cm⁻¹ for LNSAMO related to the folding mode sensitive to a change in the angle of the Mn–O–Mn bond [37–41].

These both bands are associated with the environment surrounding the MnO₆ octahedral and are related to the local modes of the MnO₆ octahedral. Two bands are sensitive to

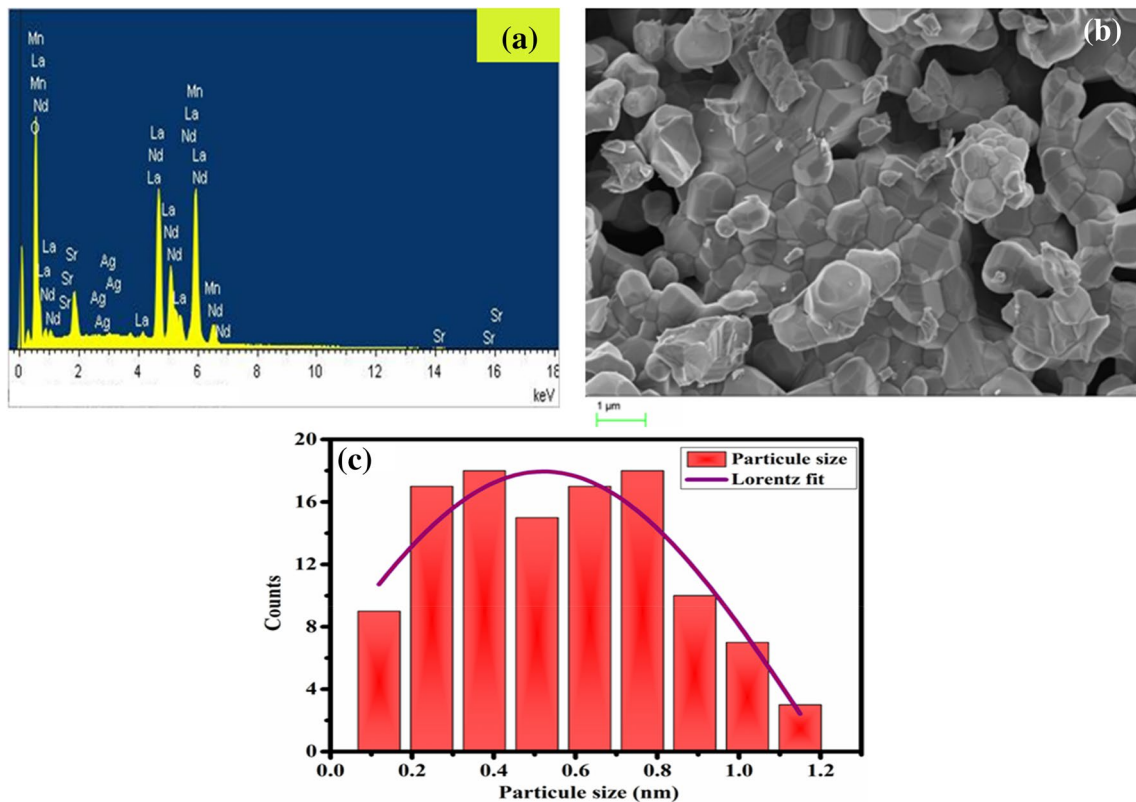


Fig. 2 **a** EDX spectra of the synthesized LNSAMO compound, **b** SEM image of surface morphologies for the LNSAMO sample, and **c** particle size distributions of the LNSAMO sample

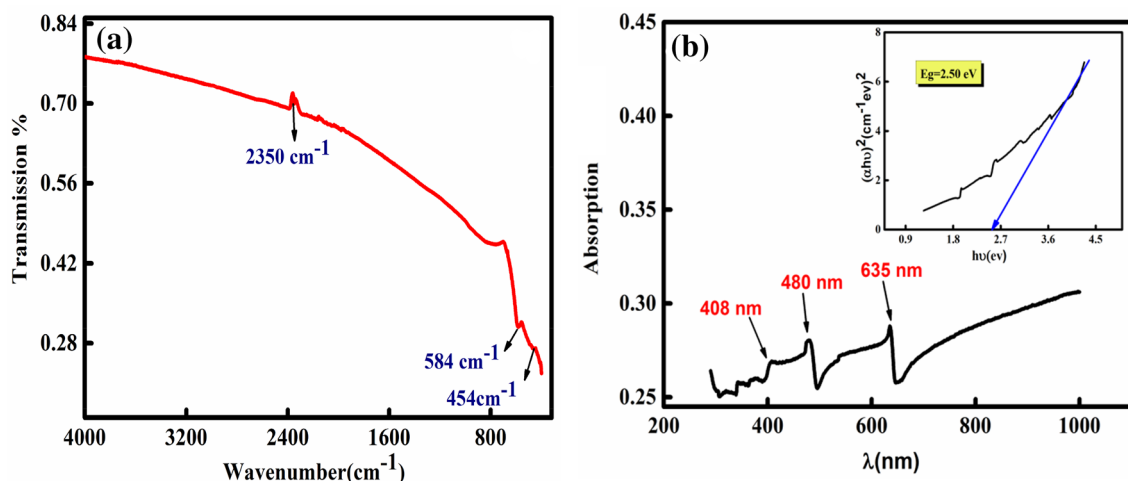


Fig. 3 **a** FTIR spectrum of perovskite LNSAMO manganite materials. **b** UV-visible absorption spectra and the inset is the plot of band gap determination for LNSAMO

octahedral distortion and lowering of symmetry resulting from the Jahn–Teller effect. The vibration band around 2350 cm^{-1} is allocated to the mode of vibratory stretching and bending of absorbed water molecules (OH) on the surface of a material [42].

3.3.2 UV-Visible absorption study

During optical absorption, the energy of the absorbed photon is given to an electron, which is, therefore, transferred from the valence band to the conduction band. Absorption can only

occur if the energy of the photon $h\nu$ is greater than gap energy (E_g). Figure 3b reveals the UV absorption spectra at room temperature for the annealed LNSAMO sample in the range 200–1000 nm, which reflects the fact that the present material can effectively absorb light over a wide range of wavelengths, including the entire visible spectrum (400–800 nm). Besides, the high absorption round 635 nm indicates that the LNSAMO sample could be a kind of photocatalysis material and photovoltaic application [43]. In addition, three strong absorption peaks centered at 408 nm (3.01 eV), 480 nm (2.43 eV), and 635 nm (1.92 eV) indicated by arrows in Fig. 3b can be attributed to the electronic transitions Mn (3d) consistent with reported behavior [44].

The energy of the optical gap of our compound is specified using the following equation of Tauc's [45]:

$$(\alpha h\nu)^n = A(h\nu - E_g) \quad (2)$$

The high absorption can generally be linked to the electronic transition from the valence band to the conduction band. However, the band gap energy is calculated by plotting the Tauc's relation [46] with the photon energy $h\nu$. The inset of Fig. 3b presents the band gap energy obtained from LNSAMO which is 2.5 eV. The absorption peaks centered at 1.92, 2.43, and 3.01 eV come from Mn transitions (3d)-electrons, while the optical band gap of approximately 2.5 eV is associated with the semiconductor behavior of LNSAMO. As this value of the optical band gap energy is greater than the theoretical value of the energy necessary for water splitting ($\lambda > 1.23$ eV) [47], our sample is, therefore, suitable for the role of solar light photocatalysts.

3.4 Magnetic properties

The study of magnetic properties gauged in a magnetic field of 0.5 T was carried out using a BS2 magnetometer. This study illustrates that our LNSAMO compound has a unique magnetic transition and behaves FM at bass temperature ($T \leq T_C$) and PM above Curie T_C temperature ($T \geq T_C$) as indicated in Fig. 4. This verifies the excellent quality of our compound. The temperature of Curie T_C determined by the derived method is presented in the insert in Fig. 4 for the LNSAMO compound from which the temperature of Curie ($T_C = 307$ K) can be established univocally. In fact, second transition at temperature about 43 K was obviously seen, which refers to the presence of the slight ferrimagnetic secondary phase Mn_3O_4 [48, 49].

The inverse magnetic susceptibility χ^{-1} (T) (specified by (H / M)) as a function of temperature for the LNSAMO compound at 0.05 T is indicated in Fig. 4. In the (PM) region, a linear fit of the curve $\chi^{-1}(T)$ as a function of T permits us to establish the Curie temperature in other manner. For a ferromagnet, it is well noted that the relation between χ and

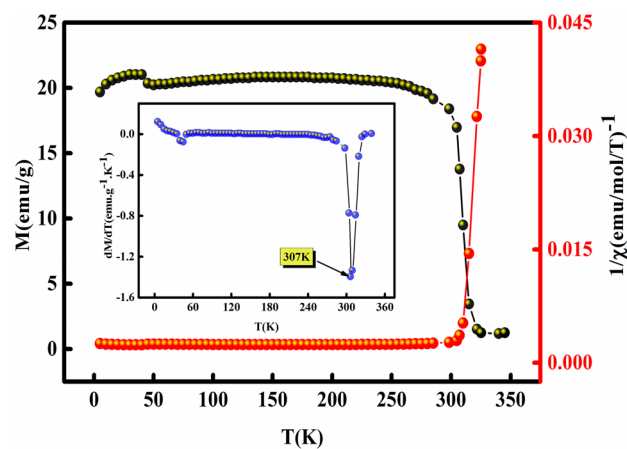


Fig. 4 Variation of the magnetization and the inverse of the susceptibility as a function of temperature at 0.05 T of the sample LNSAMO. The inset is the plot of dM/dT versus T

Table 2 Magnetic data for LNSAMO. The experimental effective paramagnetic moment μ_{eff}^{exp} , the theoretical effective paramagnetic moment μ_{eff}^{theo} , the Curie constant C, and the temperature of the curie Weiss θ_{cw}

Sample	$La_{0.57}Nd_{0.1}Sr_{0.13}Ag_{0.2}MnO_3$
T_c (K)	307
θ_{cw} (K)	308.5
C(K.uem/mol)	8.949
$\mu_{eff}^{exp}(\mu_B)$	8.461
$\mu_{eff}^{theo}(\mu_B)$	4.580

temperature T In the (PM) region should be in conformity with the Curie–Weiss (CW) law:

$$\chi = \frac{C}{T - \theta_{cw}} \quad (3)$$

where θ_{cw} is the Curie–Weiss temperature and C is the Curie constant. The line in Fig. 4 is the fitting curve inferred from b, the Curie–Weiss equation. The paramagnetic Curie temperature θ_{cw} value is of the order of 308.472 K for the LNSAMO sample. This positive value of θ_{cw} demonstrates the ferromagnetic interaction among spins.

The Curie–Weiss temperature θ_{cw} , the Curie constant C, and the effective PM moment $\mu_{eff}^{exp} = \mu_B \sqrt{8C}$ can be determined from the slope of the linear curve $1/\chi$ VS. T (Fig. 4). The effective PM moments can be calculated theoretically using this formula:

$$\mu_{eff}^{theo} = \sqrt{0.52[\mu_{eff}^2(Mn^{3+})]^2 + 0.48[\mu_{eff}^2(Mn^{4+})]^2 + 0.1[\mu_{eff}^2(Nd^{3+})]^2} \quad (4)$$

where $\mu_{\text{eff}}^{\text{the}}(\text{Mn}^{3+}) = 4.90 \mu_B$, $\mu_{\text{eff}}^{\text{the}}(\text{Mn}^{4+}) = 3.87 \mu_B$, and $\mu_{\text{eff}}^{\text{the}}(\text{Nd}^{3+}) = 3.62 \mu_B$. The Curie–Weiss temperature θ_{cw} , $\mu_{\text{eff}}^{\text{the}}$, and $\mu_{\text{eff}}^{\text{exp}}$ are highlighted in Table 2. Also, we notice that the experimental value of the PM moment $\mu_{\text{eff}}^{\text{exp}}$ is different from that calculated $\mu_{\text{eff}}^{\text{the}}$. The $\mu_{\text{eff}}^{\text{exp}}$ deduced from the fit to the CW law is considerably larger than the predicted $\mu_{\text{eff}}^{\text{the}}$ value. As a result, this difference between $\mu_{\text{eff}}^{\text{exp}}$ and $\mu_{\text{eff}}^{\text{the}}$ is probably owing to the presence of an FM correlation in the PM state, which is probably attributable to the formation in clusters FM (polarons FM).

To study other magnetic properties of the compound and to compute the variation in magnetic entropy, we realized isothermal magnetization curves ($M(H, T)$) and measurements at various temperatures in a 5 T magnetic field with a 2 K pitch. The measured isothermal magnetization with respect to the applied field in the vicinity of the Curie temperature is represented in Fig. 5. Near to the saturation and with a low magnetic field, we notice that the magnetization at low temperature increases strongly; this reveals a ferromagnetic behavior for our compound. At high fields, there is the occurrence of an indication of saturation of the magnetization. When the temperature surpasses T_C , the change of the magnetization as a function of the field becomes further linear, resulting in PM comportment. This condition as well shown in the magnetic phase transition for the LNSAMO compound.

Using the Banerjee criterion [50], we determine the nature of the transition of magnetic phase in LNSAMO and we traced the curve (H/M) par versus M^2 (which is

$$\Delta S_M \left(\frac{T_1 + T_2}{2} \right) = \frac{1}{T_1 - T_2} \left[\int_0^{\mu_0 H_{\max}} M(T_2, \mu_0 H) \mu_0 dH - \int_0^{\mu_0 H_{\max}} M(T_1, \mu_0 H) \mu_0 dH \right] \quad (6)$$

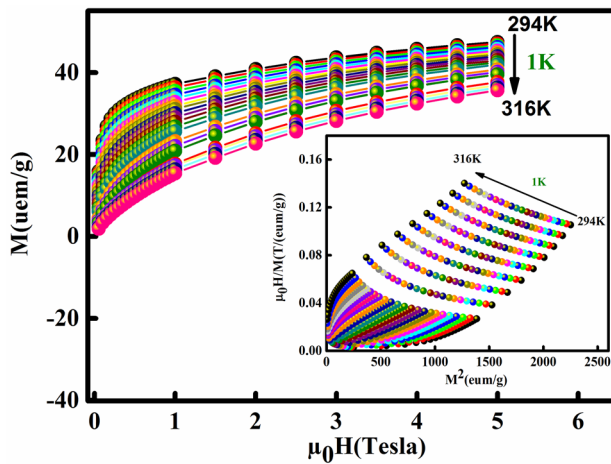


Fig. 5 The isothermal magnetization curves as a function of magnetic field. The inset displays Arrott plots (M^2 vs. $\mu_0 H/M$) for LNSAMO compounds measured at different temperatures

determined from the isotherm M vs. H (Fig. 5)) of the LNSAMO compound. Based on this criterion, it is a first-order magnetic phase transition, if the slope is negative, while it is a second-order magnetic phase transition, if the slope is positive. In this case, the slope presented in inset of Fig. 5 is positive, so we have a second-order phase transition. The mean-field estimate can be generalized to the so-entitled modified Arrott plot formula, founded on the Arrotte-Noakes equation of state [18]. An additional analysis of the magnetic phase transition may be elaborated by analyzing the critical properties of the LNSAMO compound. On the other hand, these critical exponents are not specified in the first-order transition because the magnetic field can change the transition, due to a field-dependent phase limit T_C [51].

3.5 Magnetocaloric effect

The MEC results in the heating of a material during its magnetization and its cooling during its de-magnetization. The ΔS_M caused by the change of the magnetic field from 0 to $\mu_0 H_{\max}$ is computed by the following equation: [52]

$$\Delta S_M(T, H) = \int_0^H \frac{\delta M(T, H)}{\delta T} dH = S_M(T, H) - S_M(T, 0) \quad (5)$$

Also, from the area attached between two isothermal magnetizations of the $M(H, T)$ curves, the ΔS_M can be computed, by using the following equation:

We traced the variation in magnetic entropy as a function of the temperature of the $M(H, T)$ curves (Fig. 6a) beneath different magnetic fields between 0.5 and 5 T. It is clear that the ΔS_M admits a maximum near the T_C . For the improvement of ferromagnetic interactions and the material passes from one disorderly state to another by increasing the temperature, it is noted that the absolute value of the maximum change of the ΔS_M^{\max} increases gradually with the applied magnetic field. The $|\Delta S_M^{\max}|$ value is of the order $5.08 (J \text{ kg}^{-1} \text{ K}^{-1})$ for a field of 5 T

The RCP, representing the quantity of heat transformed between the hot and cold sides in an ideal refrigeration cycle, can be expressed with [53, 54]:

$$RCP = |-(\Delta S_M^{\max})| * \delta T_{FWHM} \quad (7)$$

where ΔS_M^{\max} corresponds to the maximum ΔS_M and δT_{FWHM} correspond to the full width at half maximum. Figure 6b summarizes the RCP values and transition temperature for the LNSAMO compound. In fact, the performance

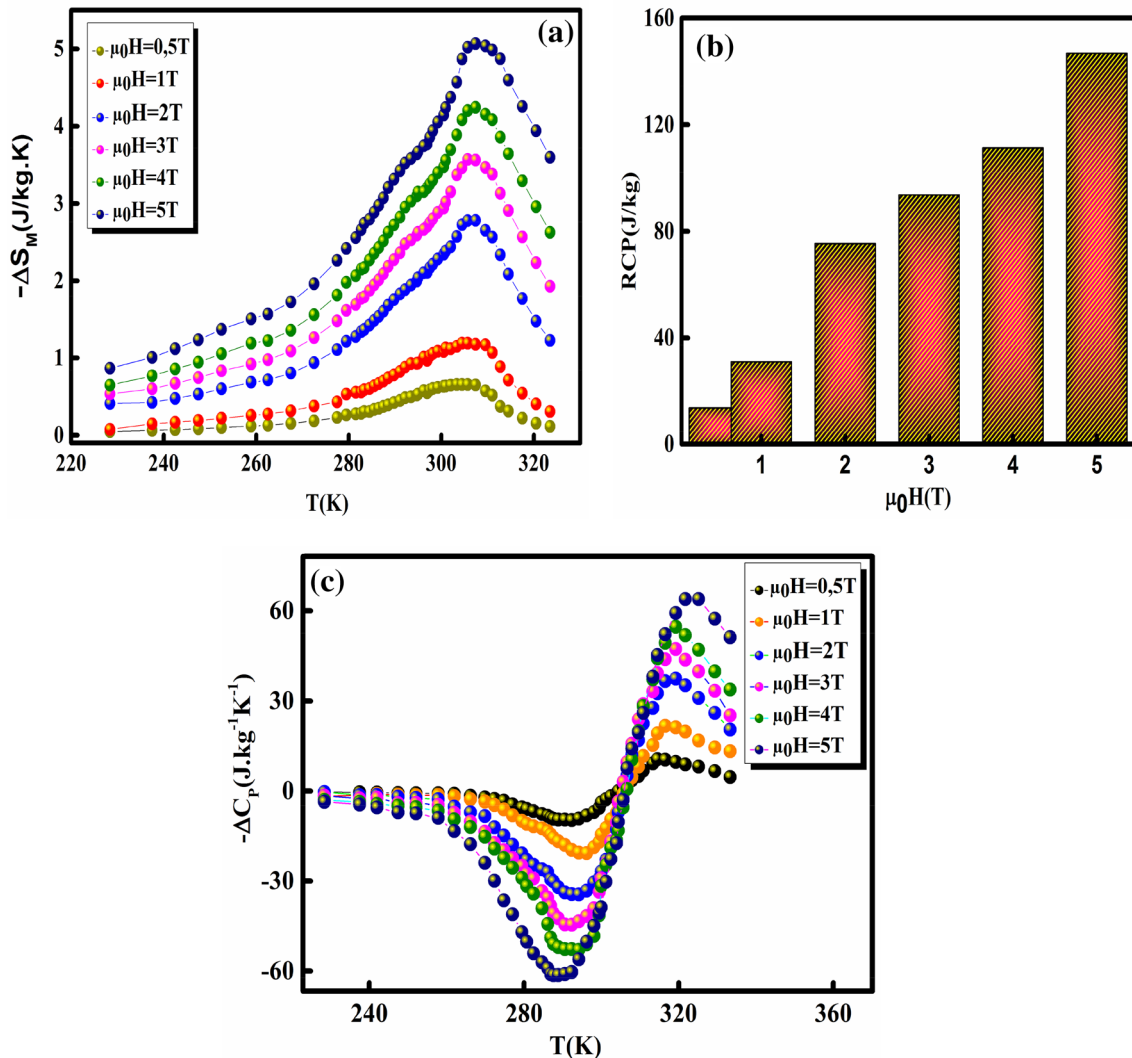


Fig. 6 **a** Magnetic entropy change, **b** Magnetic field dependence of relative cooling power values (RCP), and **c** the specific heat changes ΔC_p as a function of temperature for LNSAMO sample

of refrigeration is enhanced beneath the application of a magnetic field and a monotonous increase in RCP is determined as a function of the magnetic field of the sample, which is illustrated in Fig. 6b. The RCP at $H=5$ T is about 146.7 J kg^{-1} , corresponding to the characteristic of a good magnetocaloric material. Thus, the LNSAMO compound can be deemed as an encouraging material in magnetic refrigeration.

The variation of specific heat (ΔC_p) linked with a magnetic field change from 0 to $\mu_0 H$ is computed by ensuing equation [55, 56]:

$$\Delta C_p(T, \mu_0 H) = C_p(T, \mu_0 H) - C_p(T, 0) = T \frac{\partial[S_M(T, \mu_0 H)]}{\partial T} \quad (8)$$

Figure 6(c) reveals the dependence of the temperature with respect to the specific heat change ΔC_p for various field changes, computed from the ΔS_M data utilizing Eq. (8).

The value of ΔC_p passes rapidly from negative to positive in the vicinity of T_C and increases rapidly with increasing temperature. We find that the sum of the positive and a negative part represents the magnetic participation in the total specific heat, which influenced the heating power or cooling of the magnetic refrigerator [57].

It is noted that the maximum/minimum values of ΔC_p ($\Delta C_P^{\max}/\Delta C_P^{\min}$) rise with the application of the magnetic field, which, thus, confirms the important power of storing heat. The values of ΔS_M^{\max} , δT_{FWHM} , and RCP at different fields are computed utilizing the respective equations (Eqs. (6), (7) and (8)), which are depicted in Table 3.

Table 3 The predicted values of magnetocaloric properties for LNSAMO compound at different applied magnetic fields

Sample	$H(T)$	$-\Delta S_{max} (J kg^{-1} K^{-1})$	$\delta T_{FWHM} (K)$	$RCP (J kg^{-1})$	$\Delta CP_{max} (J kg^{-1} K^{-1})$	$\Delta CP_{min} (J kg^{-1} K^{-1})$
(LNSMAO)	0.5	0.68	45.62	13.65	11.84	- 5.81
	1	1.19	48.47	30.94	22.91	- 13.18
	2	2.97	52.06	75.33	35.79	- 31.62
	3	3.61	56.06	93.60	45.01	- 46.75
	4	4.24	64.81	111.28	50.18	- 57.08
	5	5.08	68.03	146.74	60.52	- 68.10

3.6 Critical behavior deducted from the field dependence of the magnetic entropy variation

To explore the universality class, we extracted the critical exponents of the entropy variation. We offer to extract the critical exponents from an excerpt of the field dependence of the ΔS_M .

In line to Oesterreicher and Parker [58], for secondary transition magnetic materials, the field dependence of magnetic entropy variation is described below:

$$\Delta S_M \alpha (\mu_0 H)^n \quad (9)$$

where n is assigned to a parameter characteristic of magnetic ordering [59].

Figure 7a highlights the field dependence of the magnetic entropy variation of LNSAMO simple studied by adjusting the data $\ln(\Delta S_M)$ vs. $\ln(\mu_0 H)$. The obtained value from the exponent n is 0.54 for our compound.

The field dependence of RCP is also analyzed. It can be expressed as a power law [60]:

$$RCP \alpha (\mu_0 H)^{1+\frac{1}{\delta}} \quad (10)$$

where, δ represents the critical exponent of the magnetic transition.

The variation of RCP as a function of the magnetic field is illustrated in Fig. 7b. We determined the value of δ from the fitting of $\ln(RCP)$ vs. $\ln(\mu_0 H)$ plot that corresponds to $\delta=4.30$ for the LNSAMO compound.

In the particular case at the temperature of the entropy peak ($T=T_c$), there is a mathematical relationship between the critical exponent's β , γ , and the exponent defined by [61]:

$$n(T_C) = 1 + \frac{\beta - 1}{\beta + \gamma} \quad (11)$$

The Widom relation Eq. $\beta\delta = \beta + \gamma$ [62] is formulated by the following:

$$n(T) = 1 + \frac{1}{\delta}(1 - \frac{1}{\beta}) \quad (12)$$

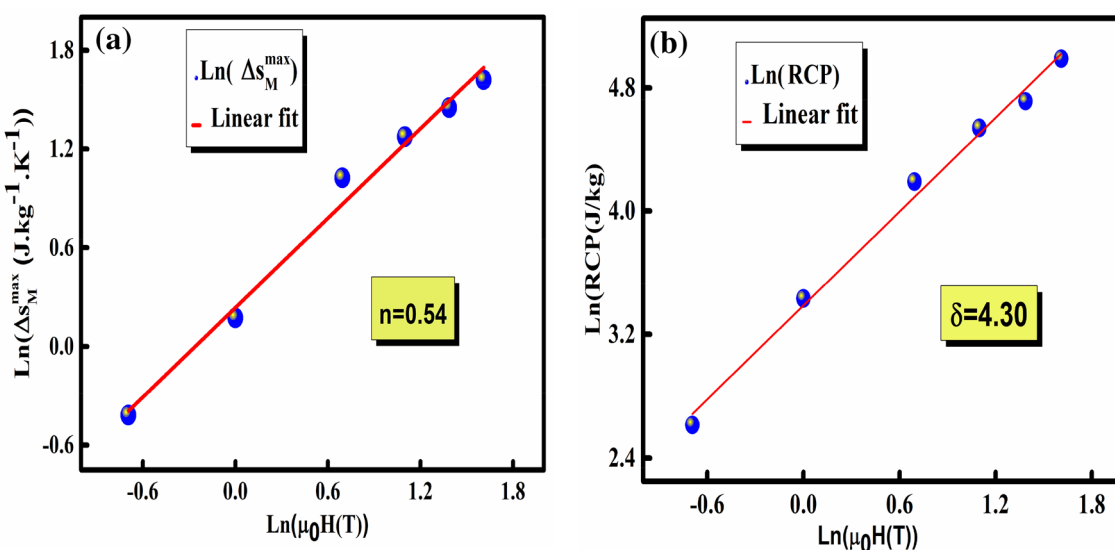


Fig. 7 Variation of $(\ln(\Delta S_M^{max}))$ vs. $\ln(\mu_0 H)$) and $(\ln(RCP))$ vs. $\ln(\mu_0 H)$) for LNSAMO compound

Using the values of n and δ deduced from the fit and the two Eqs. (11) and (12), after a well-made calculation, we find that the critical exponent's β and γ are of the order 0.335 and 1.105, respectively, for the LNSAMO sample. We note that critical exponents obtained from the field dependence of magnetic entropy variation are absolutely in good accord with those corresponding to the 3D-Ising model for LNSAMO compound.

3.6.1 Critical behavior study

We studied critical phenomena in the vicinity of the temperature of Curie T_C to interpret the nature of the magnetic phase transition for the LNSAMO sample. In conformity with the scale hypothesis, the second-order magnetic phase transition about T_C is described by a three critical behaviors, β (linked to spontaneous magnetization), γ (linked to the initial magnetic susceptibility), and δ (connected to the critical magnetization isotherm). The magnetic field can move the transition, contributing to a field-dependent phase limit T_C [51], which is why critical exponents for a first-order transition cannot be expressed.

Critical behaviors are gained mathematically, from magnetization measurements through lower asymptotic expressions [63]:

$$M_S(T < T_C, \mu_0 H \rightarrow 0) = M_0 |\varepsilon|^\beta \quad (13)$$

where $\varepsilon = \frac{T-T_C}{T_C}$ is critical amplitude and M_S is the spontaneous magnetization.

$$\chi_0^{-1}(T > T_C, \mu_0 H \rightarrow 0) = \frac{h_0}{M_0} |\varepsilon|^\gamma \quad (14)$$

$$M(T = T_C, \mu_0 H) = D(\mu_0 H) \frac{1}{\delta} \quad (15)$$

where D , M_0 and $\frac{h_0}{M_0}$ are the critical amplitudes. $\varepsilon = \frac{T-T_C}{T_C}$ is the reduced temperature.

Display in Fig. 8 are the modified Arrott plots $M^{1/\beta}$ vs. $(H/M)^{1/\gamma}$ at various temperatures utilizing several models: the Tricritical model ($\beta=0.25$, $\gamma=1$) in Fig. 8a; the mean-field model ($\beta=0.5$, $\gamma=1$) in Fig. 8b; the 3D-Ising model ($\beta=0.325$, $\gamma=1.24$) in Fig. 8c; and 3D-Heisenberg model ($\beta=0.365$, $\gamma=1.336$) Fig. 8d [64, 65]. It sounds very difficult to select which model is the most suitable to characterize our system. There exists two criteria for choosing the most suitable model: the first, all curves ought be straight and

the isotherm T_C must pass through the zero coordinate; the second, all plots must be parallel to each other and obtain the same slope. We have noticed that most models give almost straight and almost parallel lines in the high-field region.

Here, to differentiate which model identified the best, we computed their relative slopes (RS) specified in the critical point as $RS = S(T)/S(T_C)$, where $S(T)$ and $S(T_C)$ are, respectively, the slope for a indicated temperature in the vicinity of T_C and the slope $T=T_C$. The RS of the preferred model should be proximate To 1 (unit) [66]. As illustrated in Fig. 8e, the RS model of the 3D-Ising model is lot's proximity to 1 than the other models. Therefore, it can be supposed that the system can be renormalized near the 3D-Ising model.

Figure 9a displays the inverse of susceptibility ($\chi_0^{-1}(T)$) and spontaneous magnetization $M_S(T, 0)$ for this compound. From elevated fields, Linear extrapolation provides $M_S(T, 0)$ and $\chi_0^{-1}(T)$. Using Eqs. (13) and (14), new values of the critical exponents were established from the power law fitting of the $M_S(0, T)$ and $(\chi_0^{-1}(T))$ curves for LNSAMO compound. In Table 4, the values of the critical exponents of the simple as much as the theoretical values premised on various models [66, 67] are presented.

On the other side, we utilized KF method [67] to identify the values of β , γ , and T_C with great precision. The KF equations are expressed as follows:

$$M_S(T)[dM_S(T)/dT]^{-1} = \frac{T - T_C}{\beta} \quad (16)$$

$$\chi_0^{-1}(T)[d\chi_0^{-1}(T)/dT] = \frac{T - T_c}{\gamma} \quad (17)$$

Using these equations (Eqs. (16) and (17)), the $M_S(T)[dM_S(T)/dT]^{-1}$ and $\chi_0^{-1}(T)[d\chi_0^{-1}(T)/dT]$ traced against temperature must be in a straight line with slopes of $1/\beta$ and $1/\gamma$, in that order, and is exhibited in Fig. 9b for LNSAMO. The intercepts on T axis was regarded as the value of T_C . News exponents utilizing the KF method are deducted, which are also incorporated into Table 4. These results revealed that the KF values of the critical exponents and T_C are highly close to those obtained from the modified Arrott trace (MAP). As a matter of fact, it should be noted that the critical exponent values computed using the MAP method and the KF method are in excellent accord with the 3D-Ising model of the sample.

The critical isotherm $M(T, H)$ in a zone of elevated magnetic field in the proximity of T_C is utilized, to determine

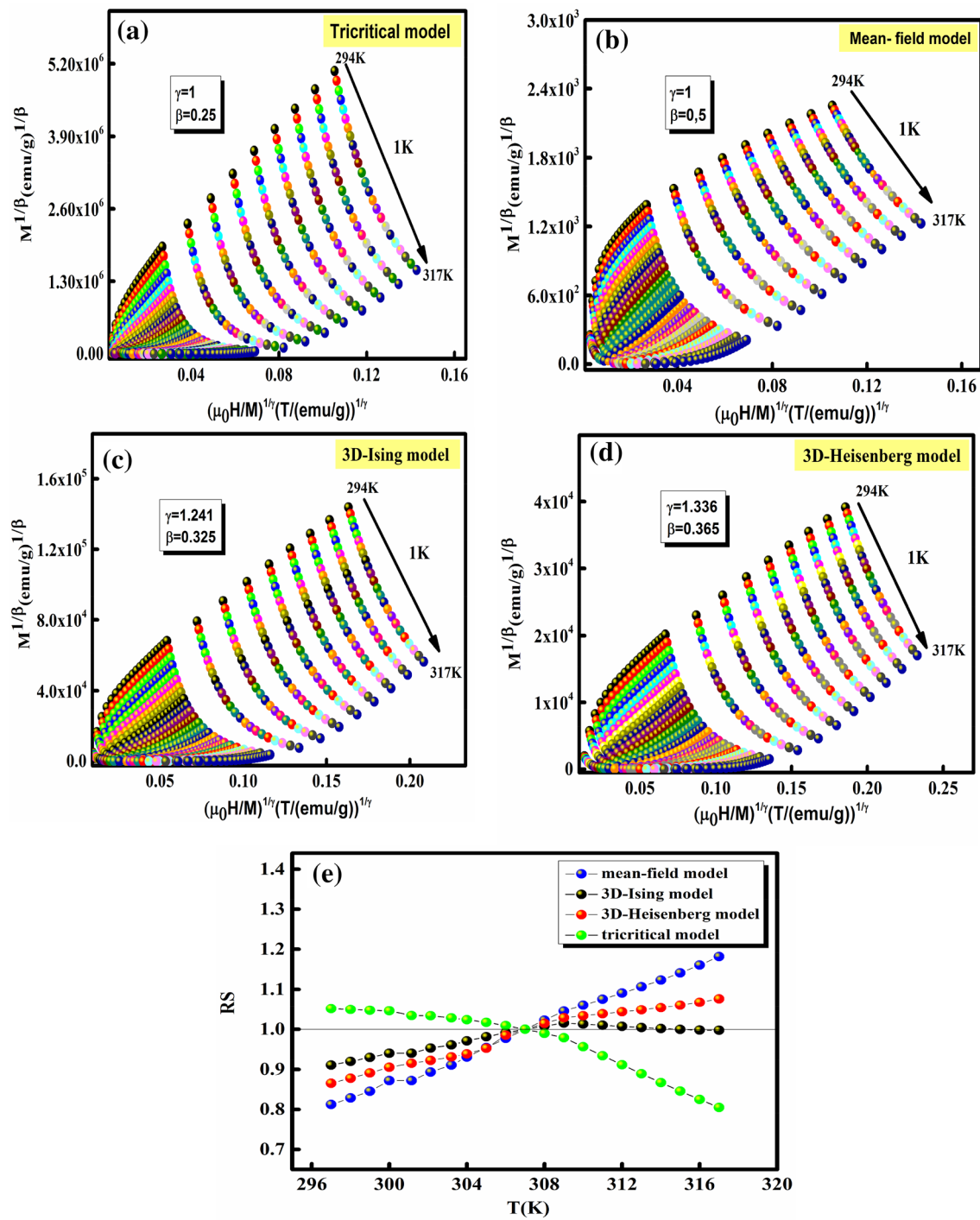


Fig. 8 The Modified Arrott plots: isotherms of $M^{1/\beta}$ vs $(\mu_0 H/M)^{1/\gamma}$ (a the tricritical model ($\beta=0.25$, $\gamma=1$), b the mean-field model ($\beta=0.25$, $\gamma=1$), c the 3D-Ising model ($\beta=0.325$, $\gamma=1.24$); d

3D-Heisenberg model ($\beta=0.365$, $\gamma=1.336$), and e the relative slope (RS) as a function of temperature defined as $RS=S(T)/S(T_C)$ for LNSAMO compound

Table 4 Values of the critical exponents of LNSAMO compound

	Technique	T_C (K)	β	γ	δ
$\text{La}_{0.57}\text{Nd}_{0.1}\text{Sr}_{0.18}\text{Ag}_{0.15}\text{MnO}_3$	MAP	299.87 ± 0.02	0.330 ± 0.003	1.099 ± 0.038	
	KF	300.26 ± 0.05	0.380 ± 0.004	0.917 ± 0.016	
	C. I (exp)				4.366 ± 0.003
	C. I (cal)				4.310
<i>Mean-field model</i>			0.5	1.0	
<i>3D-Heisenberg model</i>			0.365 ± 0.003	1.336 ± 0.004	
<i>3D-Ising model</i>			0.325 ± 0.002	1.241 ± 0.002	
<i>Tricritical mean-field</i>			0.25	1	5

C/ critical isotherm, exp Experimental, cal calculated, MAP modified Arrott plots, and KF Kouvel-Fisher

the third critical exponent δ . Figure 10a displays the critical isotherm curve at $T_C=300$ K for LNSAMO where the inset indicates the same plotting submitted in the logarithmic scale. Utilizing Eq. (18), the good fits give away the value of the exponent δ . The values found are referred in Table 4. Moreover, in line to statistical theory, the three critical exponents follow the scale relation of Widom [62]:

$$\delta = 1 + \frac{\gamma}{\beta} \quad (18)$$

Then the values obtained of β And γ are reliable and unambiguous. In order to check the accuracy of the found critical exponent values, we resort to the forecasting of the scaling theory in the critical zone expressed by the following equation:

$$M(H, \varepsilon)|\varepsilon|^{-\beta} = f_{\pm}(H|\varepsilon|^{-(\beta+\gamma)}) \quad (19)$$

where f_+ for $T > T_C$ and f_- for $T < T_C$ are regular analytic functions [68]. To guarantee the reliability of critical exhibitors, they must comply with universal scaling equations in the critical asymptotic zone. Figure 10(b) exhibits $M|\varepsilon|^{-\beta}$ vs. $\mu_0 H |\varepsilon|^{-(\beta+\gamma)}$ plot utilizing the values of β , γ , and T_C found by the KF method with the inset traced in the logarithmic scale. It is clear that the experimental data are grouped into individual branches. According to the sign ε , one is for $T > T_C$ and the other for $T < T_C$. This conclusion validates that Eq. (19) is respected more than the full range of standardized variables, which indicate the reliability of the found critical exponents and those of T_C . The critical exponents identified imply that our sample can be handled by the 3D-Ising model.

The critical exponents inferred from the ΔS_M and RCP are obviously analogous to those obtained by the KF method. This validates that the critical behavior is considerably correlated with the properties of MCE.

4 Conclusion

To sum up, we would simply assert that a detailed report on the physical properties of a LNSAMO sample was set forward. The X-ray structural analysis of our sample crystallizes in the rhombohedral structure with the $R\bar{3}c$ space group with minor traces of Mn_3O_4 . The absorption peaks centered at 408 nm (3.01 eV), 480 nm (2.43 eV), and 635 nm (1.92 eV) are related to electronic transitions Mn (3d), while the optical band gap of around 2.5 eV is associated with the semiconductor behavior of LNSAMO. The field dependence of the magnetic entropy change is investigated too, demonstrating the power law dependence $\Delta S_M \propto (\mu_0 H)^n$ where $n = 0.54$ for the compound at their respective transition

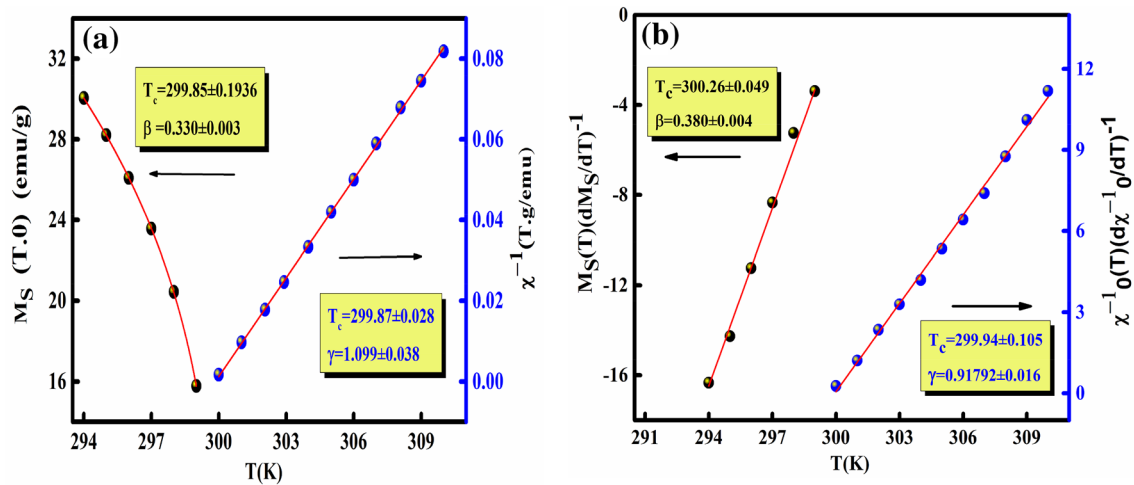


Fig. 9 **a** Temperature dependence of spontaneous magnetization (MSP) and inverse initial susceptibility (χ_0^{-1}) of LNSAMO sample. **b** Kouvel-Fisher plots for the spontaneous magnetization $M_S(T,0)$ (left) and the inverse initial susceptibility $\chi_0^{-1}(T,0)$ (right) of LNSAMO compound

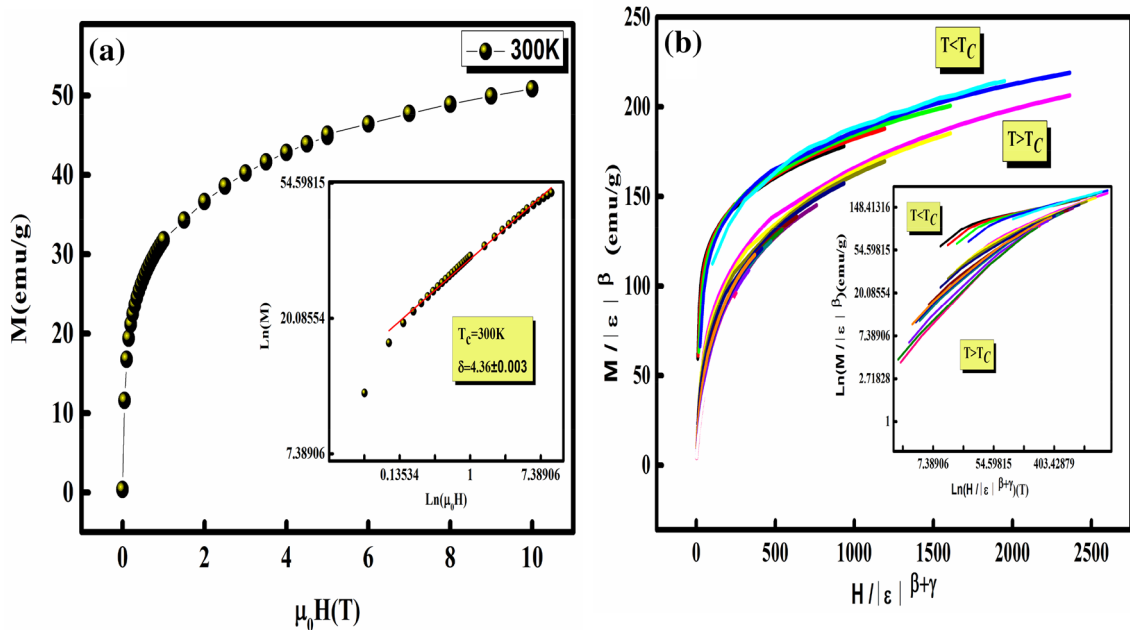


Fig. 10 **a** Critical isotherm (M vs $\mu_0 H$) for LNSAMO sample. The inset exhibits the same curve on log–log scale. **b** Scaling plots $M|\varepsilon|^{-\beta}$ vs. $\mu_0 H|\varepsilon|^{-\beta-\gamma}$ below and above T_c for LNSAMO sample. The inset exhibits the same curve on log–log scale

temperature. A good accord of the critical exponents of our compound, specified by means of isothermal magnetizations situated near T_c according to different techniques and the change of magnetic entropy. Considerable values of MCE properties near the room temperature are recorded. Arrott diagrams expose the nature of the second order of the magnetic transition in the compound. Utilizing different techniques such as the MAP, the KF method, and the CIA, the

values of β , γ , δ , and T_c are calculated. The confirmation of critical exhibitors is verified by scale analysis.

Acknowledgements The authors acknowledge the support of the Tunisian Ministry of Higher Education and Scientific Research within the framework of the Tunisian-Portuguese cooperation in the field of scientific research and technology. CFisUC is supported by national funds from FCT – Fundação para a Ciência e a Tecnologia, I.P., within the project UID/04564/2020. Access to TAIL-UC facility funded under

QREN-Mais Centro Project No. ICT_2009_02_012_1890 is gratefully acknowledged.

Compliance with ethical standards

Conflict of interest The authors declare that they have no conflict of interest.

References

1. S.K. Pal, C. Frommen, S. Kumar, B.C. Hauback, H. Fjellvåg, T.G. Woodcock, K. Nielsch, G. Helgesen, Comparative phase transformation and magnetocaloric effect study of Co and Mn substitution by Cu in MnCoGe compounds. *J. Alloys Compd.* **775**, 22–29 (2019)
2. L.H. Liu, P.Z. Liu, Y.T. Ren, X.Q. Ma, N. Chen, Y. Li, Critical behavior and magnetocaloric effect in Mn-doped Eu₈Ga₁₄Mn₂Ge₃₀type-I clathrate. *J. Alloys Compd.* **745**, 825–833 (2018)
3. K. Rudolph, A.K. Pathak, Y. Mudryk, V.K. Pecharsky, Magnetostuctural phase transitions and magnetocaloric effect in (Gd₅-xSc_x)Si_{1.8}Ge_{2.2}. *Acta Mater.* **145**, 369–376 (2018)
4. S. Jin, T.H. Tiefel, M. Mc, R.A. Cormack, R.A. Fastnacht, R. Ramesh, L.H. Chen, Thousandfold change in resistivity in magnetoresistive la-ca-mn-o films. *Science* **264**, 413 (1994)
5. K. Chahara, T. Ohno, M. Kasai, Y. Kozono, Giant magnetoresistance of a strongly correlated material La_{1-x}CaxMnO₃ film. *Appl. Phys. Lett.* **63**, 1990 (1993)
6. J.M.D. Coey, M. Viret, S. von Molnar, Mixed-valence manganites. *Adv. Phys.* **48**, 167 (1999)
7. Y. Motome, N. Furukawa, Disorder effect on spin excitation in double-exchange systems. *Phys. Rev. B* **71**(014446), 1 (2005)
8. J. Dhahri, A. Dhahri, M. Oumezzine, E. Dhahri, Magnetocaloric properties of Cd-substituted perovskite-type manganese oxides. *J. Alloys Compd.* **485**, 64 (2009)
9. I. Walha, E. Dhahri, E.K. Hlil, Magnetocaloric effect and its correlation with critical behavior in La_{0.5}Ca_{0.4}Te_{0.1}MnO₃ manganese oxide. *J. Alloys Compd.* **680**, 169 (2016)
10. I. Walha, H. Ehrenberg, H. Fuess, A. Cheikhrouhou, Structural and magnetic properties of La_{0.6-x}□_xCa_{0.4}MnO₃ (0≤x≤0.2) perovskite manganite. *J. Alloys Compd.* **485**, 56 (2009)
11. J.B. Goodenough, Theory of the Role of Covalence in the Perovskite-Type Manganites [La, M(II)]MnO₃. *Phys. Rev.* **100**(2), 564 (1955)
12. J. Kanamori, Superexchange interaction and symmetry properties of electron orbitals. *J. Phys. Chem. Solids* **10**, 87 (1959)
13. J. Kanamori, Crystal distortion in magnetic compounds. *J. Appl. Phys.* **31**(5), 14S (1960)
14. V. Goldschmidt, *International series of monographs on physics, Geochemistry* (Oxford University Press, Oxford, 1958)
15. E. Tka, K. Cherif, J. Dhahria, E. Dhahri, Effects of non magnetic aluminum Al doping on the structural, magnetic and transport properties in La_{0.57}Nd_{0.1}Sr_{0.33}MnO₃ manganite oxide. *J. Alloys Compd.* **509**, 8047–8055 (2011)
16. M.-H. Phan, S.-C. Yu, Review of the magnetocaloric effect in manganite materials. *J. Magn. Magn. Mater.* **308**, 325–340 (2007)
17. K.A. Gschneidner, V.K. Pecharsky, Magnetocaloric materials. *Annu. Rev. Mater. Sci.* **30**, 387–429 (2000)
18. L.M. Rodriguez-Martinez, J.P. Attfield, Cation disorder and size effects in magnetoresistive manganese oxide perovskites. *Phys. Rev. B* **54**, 15622 (1996)
19. E. Warburg, Magnetische Untersuchungen. *Ann. Phys.* **249**(5), 141–164 (1881)
20. A.M. Tishin, Y.I. Spichkin, *The magnetocaloric effect and its applications* (CRC Press, Boca Raton, 2003)
21. P.J. von Ranke, P.O. Ribeiro, A. Magnus, G. Carvalho, B.P. Alho, T.S.T. Alvarenga, E.P. Nobrega, A. Caldas, V.S.R. de Sousa, P.H.O. Lopes, N.A. de Oliveira, Theoretical investigation on the magnetic and electric properties in TbSb compound through an anisotropic microscopic model. *J. Appl. Phys.* **119**, 183903 (2016)
22. J.Q. Deng, J.L. Yan, J.L. Huang, J.M. Zhu, X. Chen, Y.H. Zhuang, The influence of Co substitution on the magnetocaloric effect of Gd (Al, Fe)₂. *Phys. Scripta* **75**, 604–607 (2007)
23. N. Dhahri, A. Dhahri, K.J. Dhahri, H. Belmabrouk, E. Dhahri, Effect of Co substitution on magnetocaloric effect in La_{0.67}Pb_{0.33}Mn_{1-x}Co_xO₃ (0.15 ≤ x ≤ 0.3). *J. Alloys Compd.* **507**(2), 405–409 (2010)
24. M.S. Anwar, A.A. Khan, K.Y. Park, S.R. Lee, F. Ahmed, B.H. Koo, Magnetic and magnetocaloric properties of polycrystalline Pr_{0.55}(Ca_{0.75}Sr_{0.25})_{0.45}MnO₃ compound: Observation of large inverse magnetocaloric effect. *Mater. Res. Bull.* **69**, 41–45 (2015)
25. S. Othmani, R. Blel, M. Bejar, M. Sajieddine, E. Dhahri, E.K. Hlil, New complex magnetic materials for an application in Ericsson refrigerator. *Solid State Commun.* **149**(25–26), 969–972 (2009)
26. M. Smari, I. Walha, A. Omri, J.J. Rousseau, E. Dhahri, E.K. Hlil, Critical parameters near the ferromagnetic-paramagnetic phase transition in La_{0.5}Ca_{0.5-x}Ag_xMnO₃ compounds (0.1≤x≤0.2). *J. Ceram. Int.* **40**, 8945 (2014)
27. R.H. Heffner, L.P. Le, M.F. Hundley, J.J. Neumeier, G.M. Luke, K. Kojima, B. Nachumi, Y.J. Uemura, D.E. MacLaughlin, S.W. Cheong, Physics of manganites. *Phys. Rev. Lett.* **77**, 1869 (1996)
28. M. Ziese, Critical scaling and percolation in manganite films. *J. Phys. Condens. Matter* **13**, 2919 (2001)
29. I. Walha, H. Ehrenberg, H. Fuess, A. Cheikhrouhou, Structural and magnetic properties of La_{0.6-x}□_xCa_{0.4}MnO₃ (0 ≤ x ≤ 0.2) perovskite manganite. *J. Alloys Compd.* **485**, 64 (2009)
30. A. Oleaga, A. Salazar, H. Kuwahara, Thermal diffusivity and critical behavior of Nd_{1-x}Sr_xMnO₃. *Phys. B* **512**, 378 (2006)
31. S. Taran, B.K. Chaudhuri, S. Chatterjee, H.D. Yang, S. Neeleshwar, Y.Y. Chen, Critical exponents of the La_{0.7}Sr_{0.3}MnO₃, La_{0.7}Ca_{0.3}MnO₃, and Pr_{0.7}Ca_{0.3}MnO₃ systems showing correlation between transport and magnetic properties. *J. Appl. Phys.* **98**, 103903 (2005)
32. B. Padmanabhan, H.L. Bhat, S. Elizabeth, S. Robler, U.K. Robler, K. Dorr, K.H. Muller, Critical properties in single crystals of Pr_{1-x}Pb_xMnO₃. *Phys. Rev. B* **75**, 024419 (2007)
33. J. Rodreiguez-Carvajal, *FULLPROF'98* (Laboratoire Léon Brillouin (CEA-CNRS), Gif sur Yvette Cedex, 1998)
34. J. Dhahri, A. Dhahri, M. Oumezzine, E. Dhahri, Effect of Sn-doping on the structural, magnetic and magnetocaloric properties of La_{0.67}Ba_{0.33}Mn_{1-x}Sn_xO₃ compounds. *J. Magn. Magn. Mater.* **320**, 2613 (2008)
35. J. Kanamori, Crystal distortion in magnetic compounds. *J. Appl. Phys. Suppl.* **31**, 145 (1960)
36. S. Das, T.K. Dey, Magnetic and magnetocaloric properties of the La_{0.9-x}Ag_xMn_{1.1}O₃ compounds. *J. Phys. D* **40**, 185 (2007)
37. I. Fedorov, J. Lorenzana, P. Dore, G. DeMarzi, P. Maselli, Calvani, Infrared-active phonons of LaMnO₃ and CaMnO₃. *P. Phys. Rev. B* **60**, 11875 (1999)
38. X. Wang, Q. Cui, Y. Pan, Zou, Crystal structures of C₃N₆H₆ under high pressure G. *J. Alloys Compd.* **354**, 91 (2003)
39. F. Gao, R.A. Lewis, X.L. Wang, S.X. Dou, Far-infrared reflection and transmission of La_{1-x}Ca_xMnO₃. *J. Alloys Compd.* **347**, 314 (2002)

40. F. Gao, R.A. Lewis, X.L. Wang, S.X. Dou, Infrared absorption of lanthanum manganites. *Phys. C* **2235**, 341348 (2000)
41. F. Issaoui, M. Bejar, E. Dhahri, M. Bekri, P. Lachkar, E.K. Hlil, Crystal, spinglass, Griffiths phases and magnetocaloric properties)of the $\text{Sr}_{1.5}\text{Nd}_{0.5}\text{MnO}_4$ compound. *Phys. B* **414**, 42–49 (2013)
42. M. Quijada, J.R. Černe, H.D. Simpson, K.H. Drew, A.J. Ahn, R. Millis, R. Shreekala, M. Ramesh, T. Venkatesan, Optical conductivity of manganites: Crossover from Jahn-Teller small polaron to coherent transport in the ferromagnetic state. *Phys. Rev. B* **58**, 16093 (1998)
43. M.W. Kim, J.H. Jung, K.H. Kim, H.J. Lee, J. Yu, T.W. Noh, Y. Moritomo, Spin-orbital pattern dependent polaron absorption in manganites. *Phys. Rev. Lett.* **89**, 016403 (2002)
44. X.L. Wang, D. Li, T.Y. Cui, P. Kharel, W. Liu, Z.D. Zhang, Magnetic and optical properties of multiferroic GdMnO_3 nanoparticles. *J. Appl. Phys.* **107**, 09B510 (2010)
45. L. Ben Said, A. Inoubli, B. Bouricha, M. Amlouk, Molecular and Biomolecular Spectroscopy. *J. Spectrochim. Acta Mol.* **171**, 487 (2017)
46. X. Li, Y. Hou, Q. Zhao, L. Wang, A general, one-step and template-free synthesis of sphere-like zinc ferrite nanostructures with enhanced photocatalytic activity for dye degradation. *J. Coll. Interface Sci.* **358**, 102–108 (2011)
47. K.N. Harish, H.S.B. Naik, P.N.P. Kumar, R. Viswanath, Synthesis, enhanced optical and photocatalytic study of Cd-Zn ferrites under sun light. *Catal. Sci. Technol.* **2**, 1033–1039 (2012)
48. S. Zemni, A. Gasmi, M. Boudard, M. Oumezzine, Effect of nominal strontium deficiency on the structure and the magnetic properties of $\text{La}_{0.6}\text{Sr}_{0.4-\delta}\text{MnO}_3$ manganese perovskites. *Mater. Sci. Eng. B* **144**(1–3), 117–122 (2007)
49. R. Regmi, R. Tackett, G. Lawes, Suppression of low-temperature magnetic states in Mn_3O_4 nanoparticles. *J. Magn. Magn. Mater.* **321**(15), 2296–2299 (2009)
50. B.K. Banerjee, On a generalized approach to first and second order magnetic transitions. *Phys. Lett.* **12**, 16 (1964)
51. D. Kim, B. Revaz, B.L. Zink, F. Hellman, J.J. Rhyme, J.F. Mitchell, Tricritical point and the doping dependence of the order of the ferromagnetic phase transition of $\text{La}_{1-x}\text{Ca}_x\text{MnO}_3$. *Phys. Rev. Lett.* **89**, 227202 (2002)
52. W. Zhong, W. Chen, W.P. Ding, N. Zhang, A. Hu, Y.W. Du, Q.J. Yan, Structure, composition and magnetocaloric properties in polycrystalline $\text{La}_{1-x}\text{A}_x\text{MnO}_{3+8}$ ($\text{A} = \text{Na}, \text{K}$). *J. Eur. Phys. B* **3**, 169 (1998)
53. J. Dhahri, A. Dhahri, M. Oumezzine, E. Dhahri, Effect of Sn-doping on the structural, magnetic and magnetocaloric properties of compounds. *J. Magn. Magn. Mater.* **320**, 2613 (2008)
54. V. Franco, J.S. Blazquez, A. Conde, Influence of Ge addition on the magnetocaloric effect of a Co-containing Nanoperm-type alloy. *J. Appl. Phys.* **103**, 07B316 (2008)
55. W. Zhong, W. Chen, W.P. Ding, N. Zhang, A. Hu, Y.W. Du, Q.J. Yan, Structure, composition and magnetocaloric properties in polycrystalline $\text{La}_{1-x}\text{A}_x\text{MnO}_{3+8}$ ($\text{A} = \text{Na}, \text{K}$). *Eur. Phys. J. B* **3**, 169 (1998)
56. M.A. Hamad, Great Magnetocaloric Effect of $\text{La}_{0.27}\text{Nd}_{0.4}\text{Ca}_{0.33}\text{MnO}_3$. *J. Supercond. Nov. Magn.* **27**, 223 (2014)
57. X.X. Zhang, G.H. Wen, F.W. Wang, W.H. Wang, C.H. Yu, G.H. Wu, Magnetic entropy change in Fe-based compound $\text{LaFe}_{10.6}\text{Si}_{2.4}$. *Appl. Phys. Lett.* **77**(3072), 80 (2000)
58. H. Oesterreicher, F.T. Parker, Magnetic cooling near Curie temperatures above 300 K. *J. Appl. Phys.* **55**, 4334 (1984)
59. V. Franco, J.S. Blázquez, A. Conde, Fields dependence of magnetocaloric effect in materials with a second order phase transition a muster curve for the magnetic entropy change. *Appl. Phys. Lett.* **89**, 222512 (2006)
60. A. Dhahri, E. Dhahri, E.K. Hlil, Structural characterization, magnetic properties and magnetocaloric effects of $\text{La}_{0.75}\text{Sr}_{0.25}\text{Mn}_{1-x}\text{Cr}_x\text{O}_3$ ($x = 0.15, 0.20$, and 0.25). *Appl. Phys. A* **116**, 2077 (2014)
61. V. Franco, A. Conde, M.D. Kuzmin, J.M. Romero-Enrique, *J. Appl. Phys.* **105**, 917 (2009)
62. B. Widom, Surface tension and molecular correlations near the critical. *J. Chem. Point, Phys.* **43**, 3898 (1965)
63. K. Huang, *Statistical mechanics* (Wiley, New York, 1987)
64. O. Arnache, G. Campillo, A. Hoffmann, Study of critical exponents in doped $\text{La}_{2/3}\text{Ca}_{1/3}\text{Mn}_{1-y}\text{Fe}_y\text{O}_3$ ($y=0, 0.03$) manganite films. *Appl. Phys. A* **117**, 937 (2014)
65. H.E. Stanley, *Introduction to phase transitions and critical phenomena* (Oxford University Press, London, 1971)
66. H.S. Shin, J.E. Lee, Y.S. Nam, H.L. Ju, C.W. Park, First –order-like magnetic transition in manganite oxide $\text{La}_{0.7}\text{Ca}_{0.3}\text{MnO}_3$. *Solid State Commun.* **118**, 377 (2001)
67. J.S. Kouvel, M.E. Fisher, Detailed magnetic behavior of nickel near its Curie point. *Phys. Rev.* **136**, 1626 (1964)
68. S.N. Kaul, Static critical phenomena in ferromagnetism with quenched disorder. *J. Magn. Magn. Mater.* **53**, 5 (1985)

Publisher's Note Springer Nature remains neutral with regard to jurisdictional claims in published maps and institutional affiliations.